JOURNAL OF SYNCHROTRON RADIATION

ISSN 1600-5775

Received 26 July 2018
Accepted 30 October 2018

Edited by I. Lindau, SLAC/Stanford University, USA

Keywords: surface acoustic waves (SAWs); $LiNbO_3$; standing and propagating SAW; stroboscopic XPEEM; LEEM.

Supporting information: this article has supporting information at journals.iucr.org/s

Quantification of propagating and standing surface acoustic waves by stroboscopic X-ray photoemission electron microscopy

Michael Foerster,[a]* Nahuel Statuto,[c] Blai Casals,[d] Alberto Hernández-Mínguez,[e] Simone Finizio,[f] Ania Mandziak,[a,b] Lucia Aballe,[a] Joan Manel Hernàndez Ferràs[c] and Ferran Macià[c,d]*

[a]Experiments Divison, ALBA Synchrotron, Carrer de la Llum 2-26, Cerdanyola del Valles, 08290 Barcelona, Spain, [b]Instituto de Química Física 'Rocasolano' (IQFR-CSIC), C/Serrano 119, 28006 Madrid, Spain, [c]Department of Condensed Matter Physics, University of Barcelona, 08028 Barcelona, Spain, [d]Institut de Ciència de Materials de Barcelona (ICMAB-CSIC), Campus UAB, 08193 Bellaterra, Spain, [e]Paul-Drude-Institut für Festkörperelektronik, Leibniz-Institut im Forschungsverbund Berlin eV, Germany, and [f]Institut für Physik, Johannes Gutenberg Universität, Staudingerweg 7, D-55128 Mainz, Germany. *Correspondence e-mail: mfoerster@cells.es, fmacia@icmab.es

The quantification of surface acoustic waves (SAWs) in $LiNbO_3$ piezoelectric crystals by stroboscopic X-ray photoemission electron microscopy (XPEEM), with a temporal smearing below 80 ps and a spatial resolution below 100 nm, is reported. The contrast mechanism is the varying piezoelectric surface potential associated with the SAW phase. Thus, kinetic energy spectra of photoemitted secondary electrons measure directly the SAW electrical amplitude and allow for the quantification of the associated strain. The stroboscopic imaging combined with a deliberate detuning allows resolving and quantifying the respective standing and propagating components of SAWs from a superposition of waves. Furthermore, standing-wave components can also be imaged by low-energy electron microscopy (LEEM). Our method opens the door to studies that quantitatively correlate SAWs excitation with a variety of sample electronic, magnetic and chemical properties.

1. Introduction

Surface acoustic waves (SAWs) are deformation waves at the surface, *i.e.* at the outer micrometric layer, of a crystal, which can travel macrometric distances (Auld, 1973) [see Fig. 1(*a*) for visualization]. In piezoelectric materials such as $LiNbO_3$ (LNO), SAWs can be excited by applying a radiofrequency (RF) electric signal to metallic interdigitated transducer (IDT) electrodes on the sample; if the excitation frequency f matches the spacing d of the IDT according to $f = nv/d$, where n is an integer number and v is the SAW propagation velocity, which is 3980 m s^{-1} for propagation along the X-axis of a 128° Y-cut LNO. Typical frequencies (wavelengths) are in the hundreds of MHz to low GHz (tens of micrometres to hundreds of nanometres) range. SAWs are most prominently used in commercial RF signal filters (Ruppel, 2017), in order to drive microfluidic motions in a lab-on-a-chip environment (Wixforth, 2003), as well as in research, for example for controlling light emission from quantum wells (Rocke *et al.*, 1997), driving magnetic systems (Hernandez *et al.*, 2006; Davis *et al.*, 2010; Weiler *et al.*, 2011, 2012; Thevenard *et al.*, 2016; Foerster *et al.*, 2017) or for the activation of catalytic surfaces (Mitrelias *et al.*, 1998; Inoue, 2007). Despite their frequent use and relevance, very few real-space imaging techniques (*e.g.* Kavalerov *et al.*, 2000) are available to directly observe and quantify SAWs on their intrinsic timescale.

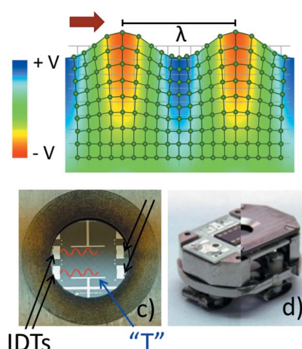

© 2019 International Union of Crystallography

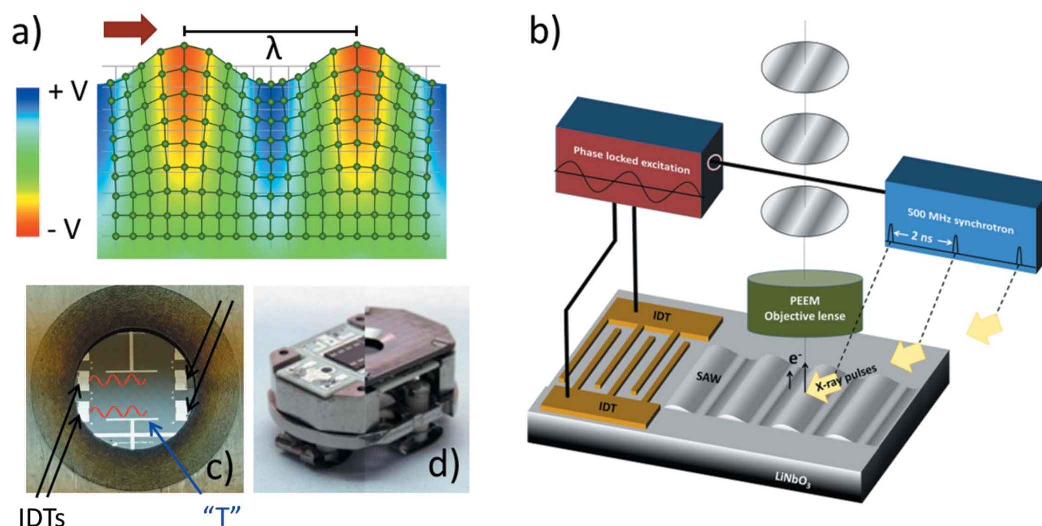

Figure 1
(*a*) Sketch of a SAW with amplitudes along the propagation direction (horizontal) and out of the plane of the crystal surface (Rayleigh mode). The amplitude along the orthogonal in-plane direction of the crystal (into the drawing plane) is zero and the wavefronts are straight. The colour shading of the background symbolizes the piezoelectric surface potential. (*b*) Scheme of the stroboscopic imaging concept: the SAWs are synchronized by an electronic phase-lock loop (PLL) to the X-ray pulses of the synchrotron, providing a perfect long-term stability with a finite single-cycle jitter. Many partial images of the sample in the same state are averaged on the 'slow' detector (on top, not shown). (*c*) Image of the sample as seen through the central hole in the cap of the sample holder. Four pairs of IDT electrodes are visible (left and right), where each pair appears as a single rectangular pattern. Additional T-shaped grounded electrodes arrive from top and bottom to reduce sample charging. (*d*) Composed image of the sample holder used for the experiment [reproduced with permission from Foerster *et al.* (2016), copyright (2016) Elsevier]. It includes a printed circuit board for wire bond contacts to the sample and a raised cap, which does not touch the sample surface to avoid short-circuiting these wires.

Here we report on the imaging of SAWs in a combined low energy–photoemission electron microscope (LEEM–PEEM) connected to the CIRCE beamline at the ALBA synchrotron (Aballe *et al.*, 2015). The beamline provides X-ray pulses of about 20 ps length at a repetition rate of 500 MHz in multi-bunch mode, which are used to excite photoelectrons from the sample surface (XPEEM). An image of the sample is formed by an electron–optical microscope based on a so-called cathode lens (Telieps & Bauer, 1985). Our system includes an imaging energy analyser in order to select at will the initial kinetic energy of the electrons used to form the image. While single-shot experiments are impossible for intensity reasons, stable snapshots of SAWs can be obtained by stroboscopic XPEEM imaging if the frequency of the continuous SAW excitation is exactly tuned to the synchrotron repetition rate of 500 MHz or one of its harmonics [see Fig. 1(*b*)]. Each X-ray pulse arrives at the sample when the SAWs wavefronts are exactly in the same place, which advances by exactly one wavelength in the time between two consecutive X-ray pulses and corresponds to one oscillation period of the SAW. Thus, integration/averaging for a single image can be performed as long as needed, typically for a few seconds. In order to change the wave position (phase) in the acquired image, an electronic delay between the synchrotron pulses and the SAW excitation can be adjusted at will.

In this article we show that the SAW electric amplitude can be directly measured by the shift of the photoelectron kinetic energy spectra, and independently tracked by a reduced charging of the LNO surface under the X-ray beam at high SAW power. From the electric amplitude, the associated strain can be calculated. The stroboscopic method, together with a small deliberate detuning, also allows for a quantitative analysis of propagating and standing components of SAWs. The method can be used to investigate SAWs in detail in very specific configurations and, thus, may not only help in the design of future SAW devices but also provide the grounds for studying SAW-excited mechanisms in versatile LEEM/PEEM instruments, triggered either by the varying induced strain or by the varying electric component.

2. Experimental setup

Sample charging is critical in LEEM–PEEM and strong limitations can be expected when trying to work with a bulk piezoelectric crystal like LNO. Therefore samples were prepared on pieces of 'black' 128° *Y*-cut LNO wafers (see http://www.roditi.com/SingleCrystal/LiNbO3/liNBO3-Black-Wafers.html), which provides a single axis for efficient SAW excitation and propagation. Even so, it was necessary to reduce the beamline flux by up to two orders of magnitude compared with the usual optimized conditions in order to be able to image the sample.

Samples were prepared with unidirectional IDTs, patterned by photolithography and deposited with electron beam evaporation (10 nm Ti/40 nm Al/10 nm Ti), defining a fundamental SAW Rayleigh mode of approximately 32 µm wavelength. The geometry was designed so that the frequency of the fourth harmonic matches the synchrotron frequency of approximately 499.654 MHz. Fig. 1(*c*) shows photographs of the sample visible through the central hole of the sample

holder top cap (hole diameter 8 mm). A total of four pairs of IDT structures are visible, appearing in the photograph as single rectangles; the SAW propagation direction is horizontal in the image. Additional T-shaped electrodes (Al, 100 nm, defined by electron beam lithography) connected to the sample holder ground potential have been added at the top and bottom to further reduce sample charging. The geometry with opposite IDTs, apart from being used for electrical characterization of the device (RF transmission), gives the possibility to create interference patterns such as standing SAWs, which will also be addressed in this manuscript.

The samples are mounted into a custom sample holder [see Fig. 1(*d*) and Foerster *et al.* (2016)] which includes a printed circuit board (PCB) to provide a platform for wire bonds to the IDT contact pads. Short wire connections between the sample holder feet and the PCB were realized using thin Cu wires and silver paste. The cap is raised slightly above the sample surface in order to avoid short-circuiting the bond wires. This raised cap configuration can produce imaging artefacts due to an electrostatic lens effect of the hole in the cap, constraining the useful area to the central region of the sample. In general this was found to be a more severe limitation than the shadowing of the grazing-incidence X-ray beam. In order to reduce the risk of arcing between the sample and the objective lens, the microscope was operated at a reduced 10 kV main acceleration voltage and samples were degassed in ultrahigh vacuum at low temperatures (<100°C) for at least 1 h prior to the measurements.

The basic electronic system to produce the RF excitation signal for SAWs in the PEEM microscope is described in detail elsewhere (Foerster *et al.*, 2016). It basically consists of an RF function generator to produce an analog sinusoidal signal, which is phase-locked to the synchrotron master clock and can be adjusted in amplitude and phase. This signal is transmitted by an optical fibre, providing galvanic separation, into the PEEM high-voltage rack and amplified [maximum power 41 dBm (dBm: decibels relative to one milliwatt)]. Recently, a two-channel version with independent amplitude and phase has become available (Molas *et al.*, 2017). The cable between the rack and the sample UHV manipulator at the microscope has been upgraded to a coaxial type RG 178 while maintaining the original UHV feedthrough as well as the spring-type electrical contacts between the sample holder and the manipulator head. While the bandwidth of the electronic setup alone (diodes and receivers) ranges from 100 to 1000 MHz, the signal is increasingly attenuated at higher frequencies by the cable and the UHV feedthrough, which is a non-high-frequency component. A setup to diagnose the IDT connection status of the sample inside the PEEM manipulator is explained in Section S1 of the supporting information. At the higher power levels used, a slow spatial drift of the SAW features on the sample is observed after changing the excitation power level. We ascribe this drift, which can extend over up to 1–2 h, to a temperature change of the LNO surface, which consequently changes the wavelength λ for a given frequency. Measurements were started at each power after stabilization. As shown in Appendix *A*, the time-resolved imaging of the SAWs allows estimation of an upper limit of the overall experimental jitter or time resolution of about 80 ps, an excellent value for time-resolved PEEM.

3. Results

3.1. Contrast mechanism and SAW amplitude measurement

Fig. 2(*a*) shows the direct XPEEM image of a synchronized 500 MHz SAW measured under the pulsed synchrotron X-ray illumination, integrating for 10 s. The clearly visible SAW contrast (λ = 8 µm) is independent of the X-ray photon energy or polarization, but strongly depends on the bias voltage, V_B, applied to the sample with respect to the microscope objective in order to extract the photoelectrons [−3 V in Fig. 2(*a*)]. Note that any local surface potential caused by beam-induced charging and, importantly, SAW electric potential may affect the kinetic energy of the photoelectrons, which is scanned with the V_B. For the purpose of this discussion, only the relative values between identical conditions are important. We show in Fig. 2(*b*) an image of the same area and SAW conditions, but acquired at V_B = 0.5 V. The contrast between the two images, Figs. 2(*a*) and 2(*b*), is fully inverted. By scanning the photoelectron kinetic energy by varying V_B we observe a gradual change of the contrast and indeed we can extract local spectra of the detector counts as a function of V_B at positions with different SAW phases. In Fig. 2(*c*), we show spectra corresponding to different locations, marked with red and blue squares in Fig. 2(*a*). The vertical lines mark the conditions in which Figs. 2(*a*) (solid line) and 2(*b*) (dashed line) were recorded. The spectral shift from one position of the sample to another explains the contrast inversion between Figs. 2(*a*) and 2(*b*) as either one or the other spectra shows more intensity at the marked value of V_B. Since all other parameters are the same over the whole area (photon flux, SAW excitation amplitude), we ascribe the shift of the photoelectron emission spectrum to the local SAW phase, *i.e.* to the local piezoelectric surface potential that accompanies the SAW deformation wave [visualized in Fig. 1(*a*) as a colour scale of the background].

The local shift of the photoelectron spectra allows for the local quantification of the electric amplitude of the SAW in the microscope field of view: the spectral shift between SAW extreme points directly measures the amplitude of the SAW-induced surface potential. Results obtained at different SAW excitation amplitudes are summarized in Fig. 2(*d*)[1]. The

[1] To calculate this nominal excitation SAW amplitude, an offset power factor of −24 dB is introduced between the amplifier output and the power arriving at the IDT, which summarizes the effect of several factors which cannot be reliably measured, like the high-frequency connectivity of the UHV feedthrough and sample holder, the conversion efficiency of the IDTs from the electrical signal into SAW as well as a damping/loss of SAW intensity until it reaches the area imaged by the microscope. Note that an offset power in dB, *i.e.* on a logarithmic scale, does not affect the shape of the curve described by the represented data, but rather introduces a scaling factor on the *x*-axis. The chosen value of −24 dB compares with approximately −17 dB from the electrical cable and contacts characterization (at 500 MHz) when replacing the sample by a short circuit in the PEEM sample stage and is consistent with the appearance of distortions in the RF signal appearing at the specified maximum output power of the RF amplifier.

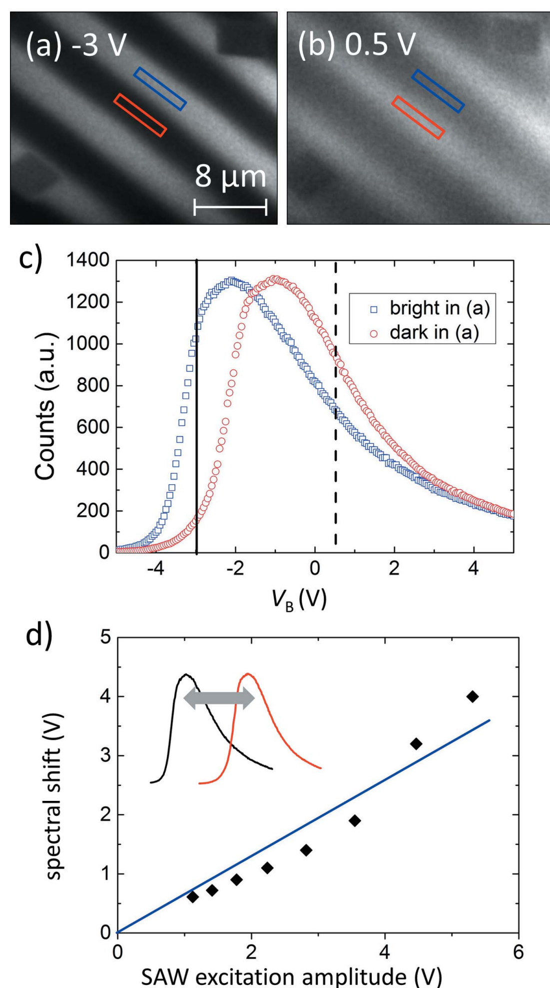

Figure 2
XPEEM images of a SAW at bias voltage, V_B, of (*a*) −3 V and (*b*) +0.5 V. The photon energy ($h\nu$ = 848 eV), the total exposure time (10 s) and the size (~30 µm × 23 µm) are the same for both. In the lower left and upper right corners of the images the same alignment markers are visible as dark squares. (*c*) Bias voltage, V_B, scans for the centres of the bright and dark stripes in the image of part (*a*). The solid and dashed vertical lines represent the conditions at which the images in (*a*) and (*b*) were recorded. (*d*) Splitting between the local spectra as a function of the applied SAW excitation amplitude; the blue line is a guide to the eye.

measured voltage difference is indeed proportional to the SAW excitation amplitude, as expected, since we are, in principle, in the linear regime for the transducers and amplification system. In summary, the local SAW-induced surface potential is measured (*i.e.* accounting for all possible losses and inhomogeneities), and thus the local strain caused by the SAW can be precisely determined (Auld, 1973).

It is known that surface charging of insulating and semiconducting samples is a pertinent issue in XPEEM as it can shift considerably the measured photoelectron spectra depending on the absorbed X-ray intensity. In order to exclude artefacts in the measured SAW-induced surface potential due to differential charging, we recorded photoelectron kinetic energy scans (as in Fig. 2) at fixed SAW amplitude but changing the incoming X-ray beam intensity (the main origin of the surface charging). Results are summarized in Fig. 3(*a*): the SAW-induced surface potential extracted from spectra for opposite extreme SAW phases is plotted as a function of the beamline refocusing mirror drain current in pA, which measures the beam intensity (1 pA corresponds to roughly 2.3 × 10^8 photons s^{-1}). The intensity used is low: 250 pA in drain current corresponds to about 2.5% of the maximum beamline intensity.

The measured SAW-induced surface potential (black squares) is independent of the beam intensity whereas the local photoelectron spectra curves shift together in V_B, indicating an increase in averaged surface charging (blue squares points). We note here that data in Fig. 3(*a*) correspond to a different sample and thus the obtained values for SAW-induced surface potential are not fully comparable with Fig. 2.

We also analysed the surface charging as a function of the SAW excitation amplitude using data shown in Fig. 2(*d*). Interestingly, there is a clear correlation between SAW power and charging, as shown in Fig. 3(*b*). The plotted value is the averaged nominal electron energy shift of a large zone (comprising roughly equal areas of all SAW phases) with respect to the value expected for a conducting sample. Thus, a decreasing value indicates less charging of the LNO substrate at constant incident beam intensity. The reduced charging with

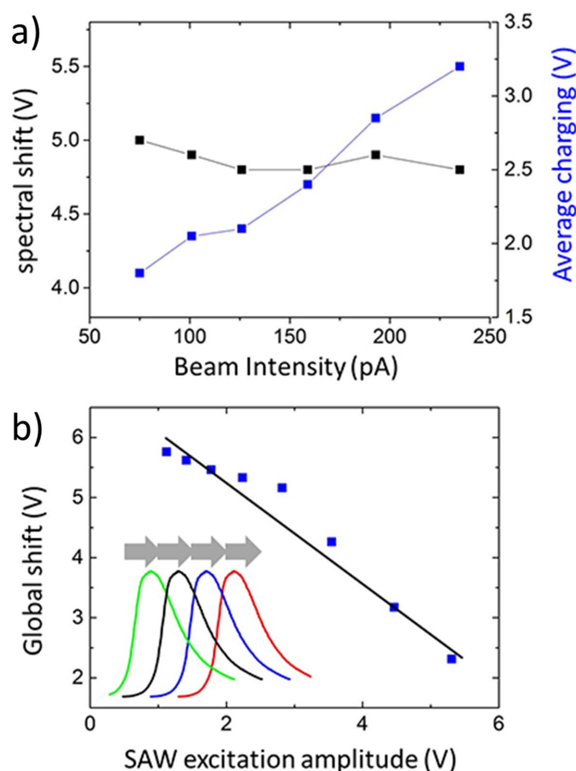

Figure 3
Surface charging of the $LiNbO_3$ substrate under the synchrotron X-ray beam. (*a*) Shift between the two extreme spectra, indicating the amplitude of the SAW (black squares), and parallel shift of the two spectra, indicating an increase of surface charging (blue squares), as a function of the beam intensity at constant SAW excitation amplitude. (*b*) Global shift (averaged over a sample area containing equal content of all SAW phases) for the same data set as shown in Fig. 2 as a function of SAW excitation amplitude, indicating a reduction of charging at increasing SAW power.

SAW power, regardless of whether it is due to a higher conductivity of the LNO due to heating or due to more subtle mechanisms such as SAW-assisted charge transport, provides an independent, simpler and faster method to assess the SAW amplitude in the investigated region. In fact, the data plotted in Figs. 2(*d*) and 3(*b*) show similar deviations from ideal linear dependence, although they are different quantities, which could indicate a SAW amplitude variation in the experiment with respect to the nominal applied power.

3.2. Quantifying mixed propagating and standing SAWs

Further experimental opportunities are offered by the creation and control of standing SAWs (SSAWs) in addition to propagating SAWs (PSAWs). SSAWs provide different locations in the sample where certain strain components either oscillate or remain unchanged, *i.e.* they allow stabilizing spatial patterns (alternating nodes and antinodes) over any desired period of time (much longer than the SAW period). SSAWs can be generated by exciting two opposite IDTs (Beil *et al.*, 2008) or by the reflections created in opposed IDTs in resonant structures (de Lima *et al.*, 2012). In fact, in experiments one must deal with a superposition of standing and propagating waves (Kuszewski *et al.*, 2018). In the following, we describe a method to disentangle and quantify mixtures of SSAWs and PSAWs, which may offer a systematic way of optimizing experimental conditions.

On the one hand, static measurements — meaning not synchronizing the SAWs with the X-rays (or any other probe) — are sensitive to the SSAWs only, with an indirect signal possibly derived from averaging over all phases if the contrast is a non-linear (non-odd symmetry) function of amplitude. In principle, such a signal can be optimized, but still the relative strength of the two components is unknown. On the other hand, the stroboscopic XPEEM imaging alone does not distinguish PSAWs from SSAWs and produces equivalent snapshots. However, by combining it with a small detuning ($\Delta f \simeq 0.1$ Hz) of the SAW excitation with respect to the synchrotron repetition rate, characteristic patterns can be observed. Videos acquired with small detuning are effectively a phase scan with time-dependent phase lag of $\Delta\phi = 2\pi/\Delta f t$ and can be used as well to evaluate the propagation direction of a PSAW (Foerster *et al.*, 2017).

Videos consisting of many images of the detuned SAWs are analysed in order to obtain the SSAW and PSAW components. Two of the videos, Video S1 and Video S2, are presented in the supporting information, illustrating the time-dependent patterns for two different situations: (i) only one IDT excited and (ii) two opposing IDTs sourced with equal SAW excitation amplitude. Both cases result in a λ = 8 µm periodicity in a single image, corresponding to a phase-resolved image of either a standing or propagating SAW, but there is a clear difference between the sequences: the SAWs appear to move forward in the case of a single IDT, whereas the intensity collectively oscillates when two IDTs are used.

For a pure PSAW, the time-dependent intensity oscillations for all pixels should have equal amplitude and vary continuously in phase along the propagation direction. In contrast, for a SSAW, the intensity oscillations for all pixels should be in phase but show varying amplitudes, vanishing at the nodes. We calculated pixelwise the fast Fourier transform (FFT) of the videos and determined amplitude and phase at a fixed frequency f_0. Results of this operation are summarized in Fig. 4 for the two cases presented in the video, which are expected to correspond to a dominating propagating and standing character of the SAW, respectively.

In Fig. 4(*a*), maps of the local FFT amplitude for one (left) and two (right) excited IDTs are shown together with profiles taken inside the indicated boxes (below). A clear spatial dependence with pronounced nodes and $\lambda/2$ = 4 µm periodi-

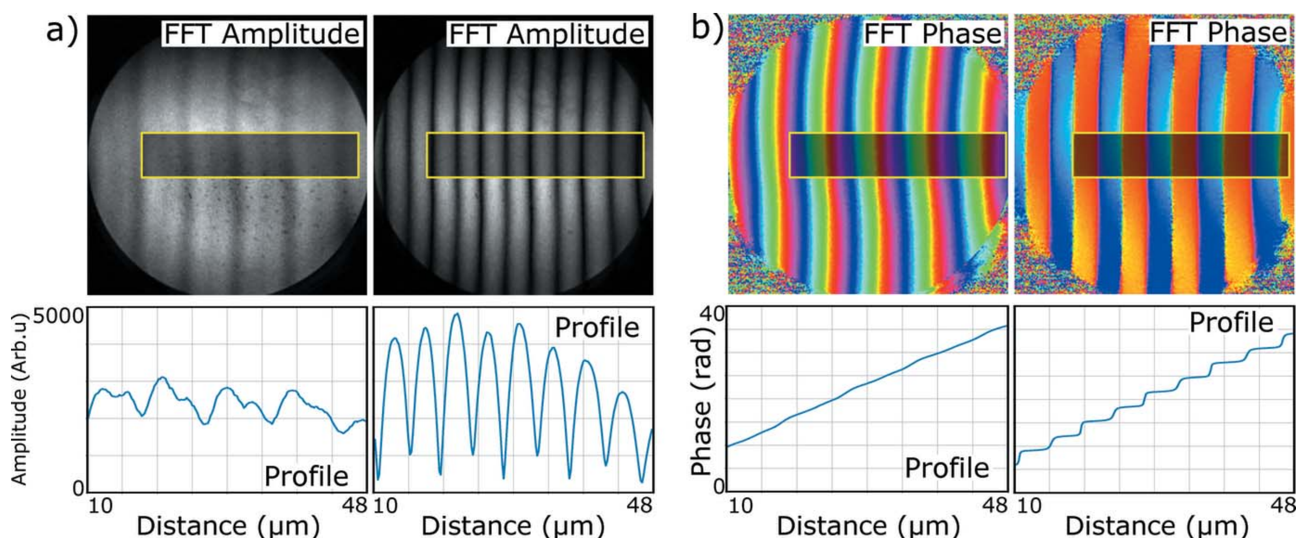

Figure 4
Results of the fast Fourier transform (FFT) analysis of the SAWs from videos shown in the supporting information. (*a*) FFT amplitude maps for excitation of one (left-hand side) or two IDTs (right-hand side). The profiles below the maps were extracted from the highlighted box. (*b*) Corresponding maps (in periodic colour scale) and profiles of the FFT phase parameter.

city can be appreciated in the configuration for SSAWs (right-hand side panel). In contrast, in the single IDT configuration (left-hand side panel), rather than a constant amplitude, a small modulation is observed, displaying mixed λ = 8 µm and $\lambda/2$ = 4 µm periodicities. This indicates a finite SSAW component within a dominantly PSAW, arising from reflections at the opposite resonating IDT. In Fig. 4(*b*), the corresponding maps for the local FFT phase in periodic colour scale are shown. The propagating SAW (left) shows the expected continuous increase of the phase along the propagation direction. On the right-hand side, the phase profile exhibits phase jumps of π at each node, which, taking into account the 2π periodicity, reflects the standing wave character.

This method allows for the quantification of arbitrary mixtures of SSAWs and PSAWs, expressing the relative strength of the propagating and standing wave component by the ratio $r_{\rm ampl} = \min(A)/\max(A)$, where min and max refer to the minimum and maximum of the FFT amplitude, A, within the map. For example, for a pure propagating wave, the FFT amplitude A is constant and $r_{\rm ampl} = 1$, while for a pure standing wave $\min(A) = 0$ and thus $r_{\rm ampl} = 0$. For a general wave superposition, the ratio $r_{\rm ampl}$ is the relative content of a propagating wave. The equivalent ratio when defined on the basis of the FFT phase ϕ is: $r_{\rm phase} = [\min(D)/\max(D)]^{1/2}$ where D is the spatial derivative of the phase $D = |\partial\phi/\partial x|$. We can, thus, extract the value for the propagating wave component, $r_{\rm p}$, from experimental parameters.

We have applied the analysis to a series of datasets with fixed excitation power on one IDT (−27 dBm) and varying excitation power on the opposite IDT. Notice here that power values are nominal values applied to the function generator and power to the sample might be about 30 dB higher. A SSAW is expected for equal power on both IDTs, while an increasing propagating character is expected when the two IDTs have different powers. In Fig. 5, $r_{\rm p}$ values extracted from the FFT analysis of the detuning movies are summarized. Black squares correspond to values determined from FFT amplitude maps, while red dots correspond to values determined from FFT phase maps. Indeed, the data show an extended region with very little propagating wave content close to equal nominal power and increasing propagating character at different power levels. The blue line is a fit to the data with a function $f(V_2) = |2V_1/(V_1 + V_2) - 1|$, where V_i is the amplitude of the signal from IDT i. We considered V_1, the amplitude of the signal from the IDT with fixed power, as a fit parameter and the function was fitted in V_2. We obtained a good description of the data and the fit parameter for the amplitude V_1 = −27.9 dBm, close to the nominal value of −27 dBm. Deviations from nominal equal powers can arise from variations in the connections and/or IDT quality as well as the exact location on the sample resulting in different damping of the SAW between the IDTs and the measured region, highlighting the convenience of a local, quantitative method for disentangling propagating and standing contributions.

Another parameter to account for when generating SSAW from two counter-propagating PSAW is the relative phase

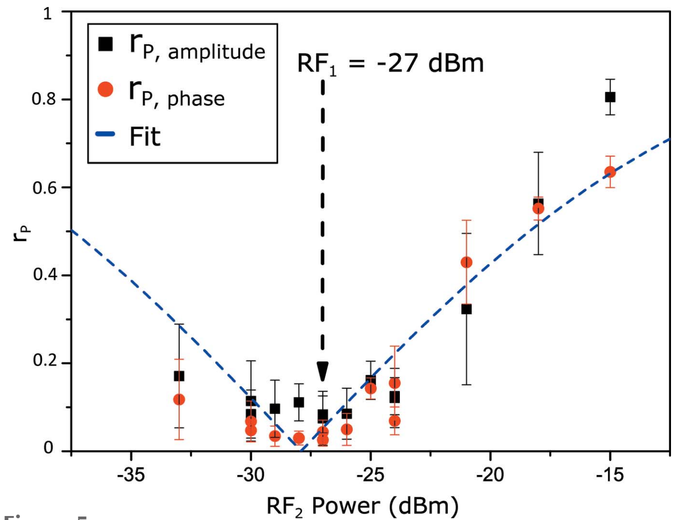

Figure 5
Determined propagating wave character in the superposition of two counter-propagating SAWs from opposing IDTs. The first IDT is kept at a fixed nominal power of −27 dBm, while the power at the second IDT is varied. Black and red squares (dots) give the propagating wave content determined from FFT maps of the amplitude and phase of recorded detuning 'movies' as explained in the text. The blue line is a one-parameter fit to the data, revealing the difference between the points of nominal and real power balance.

between the RF signals at the two opposing IDTs. The main panel of Fig. 6 depicts two profiles of the FFT amplitude for equal signal amplitude from the two IDTs but with a different relative phase: 40° (black data) and 220° (blue data). As expected, the nodes and antinodes are rigidly displaced by about 2 µm. The upper left inset panel shows the evolution of the two peaks marked green and yellow in Fig. 6 as a function

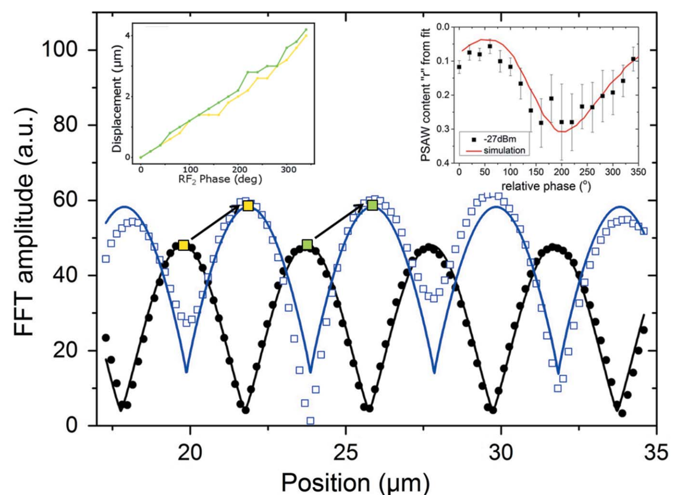

Figure 6
Profiles calculated from the FFT amplitude for RF1 and RF2 at the same power (−27 dBm). The black data show the profile when the phase of RF2 is 40° and the blue for 220°. The green and yellow markers highlight the displacement of the maxima, as shown in the upper-left inset from 0 to 360°. In the upper-right inset, the remaining propagating content in the SSAWs, determined by fits to the FFT profiles (*e.g.* black and blue line in the main panel), is plotted as a function of the relative phase. The red line in the inset results from a mathematical simulation using the application described in the supporting information.

of the relative phase between the two IDT signals. Both peaks present a parallel displacement, with a distance of ∼4 μm, which matches half of the SAW wavelength. Thus, by tuning the relative phase of the exciting RF signal at the two IDTs, either a node or antinode can be selectively placed in a desired spot in the microscope field of view of the sample, which allows us to create and control a highly local (periodic) excitation mode with submicrometer resolution in the sample.

However, the relative phase between the two IDT signals not only varies the position of the nodes of the SSAW but, importantly, it also changes the quality of the SSAW due to the reflections created in the IDT. As shown in Appendix *B*, opposed IDTs induce a reflection of an incoming resonant SAW signal with only a weak dependence on whether the IDT is terminated by a short circuit, open circuit or with a standard 50 Ω load. Therefore, when signals are applied simultaneously at both IDTs for counter-propagating SAWs, one has to consider as well the respective reflections. In the most favourable case the reflection is in phase with the generated signal and only contributes to increase the overall signal amplitude. However, if the reflected signal has even a small phase difference, *e.g.* if the distance between the IDTs does not match exactly a multiple of λ (which slightly varies with the sample temperature T and thus is difficult to control for all SAW power levels), more complex SAW superposition will occur.

We recorded detuning movies and performed FFT analysis for a dataset of nominal equal power varying the relative phase in steps of 20°. The data in the main panel of Fig. 6 correspond to two extreme cases (40° and 220° relative phase) and show a clear difference. For the black data (40°) the shape of the FFT amplitude indeed resembles that of a nearly ideal SSAW, while for the blue data (220°) recognizable deviations occur, such as the variation of the node depth. All resulting FFT amplitude profiles $A(x)$ were fitted with a function $f(x) = C + Dg(x)$ containing a constant term C and an oscillating term with amplitude D and generic shape $g(x) = [\sin^2(2\pi x/\lambda)]^n$. The exponent n was treated as a fit parameter and varied between 0.4 and 0.7; note that the exact shape of $g(x)$ *a priori* cannot be known since the XPEEM intensity is a non-linear function of SAW amplitude. Fits for the data in Fig. 6 are shown as continuous lines. From the relative strength of the oscillating term D and the constant term C, the relative content of PSAW, r, as defined before can be calculated as $r = C/(C + D)$, serving as an indication of the purity of the SSAW: a higher r value indicates more PSAW contribution. The parameter r is plotted for all measurements in the upper right inset of Fig. 6, showing a surprisingly large variation of the purity of the generated SSAW as a function of the relative phase between the RF signals applied at the opposite IDT. This ratio oscillates between about 0.1 for the best SSAW patterns at relative phases between 20° and 60° and up to approximately 0.3 at relative phases around 200° at constant relative power level. Comparison of this finding with the data shown in Fig. 5 reveals that the influence of the relative phase is considerable and in fact larger than that of a small power mismatch. We also provide an interactive code that allows mathematical generation of SSAW patterns from two IDTs with variable phases and powers in the supporting information as web application (explanation in Section S3 of the supporting information). The red line in the upper right inset of Fig. 6 was generated with this application with realistic parameters (amplitude bias 16%, relative position 0.1 and reflection 0.2), showing that the observed behaviour is plausible. To conclude this section, we stress again the importance of the relative phase of the RF signals applied to opposing IDTs when generating SSAW from two counter-propagating SAWs: it allows the desired location of SSAW nodes and antinodes to be selected with submicrometer resolution on the sample, but also influences the purity of the SSAW, constituting a parameter that can be optimized.

Finally we mention the possibility to observe SAW by the associated LEEM technique, which is integrated in many XPEEM instruments. In principle a SSAW component can always be imaged by any non-synchronized or even static method as long as the measured intensity as a function of SAW amplitude $I(a)$ is a non-odd symmetric function and, thus, $I(a) + I(-a) \neq 2I(0)$. The PSAW part, on the other hand, becomes undetectable upon large detuning or complete lack of synchronization. An example of non-synchronized imaging is to use the LEEM electron gun as a continuous electron illumination source. In particular, at electron energies close to the transition between mirror electron microscopy (MEM) and LEEM, imaging is very sensitive to changes of the sample workfunction or surface potential. In Fig. 7(*a*) an image of a 500 MHz SAW in $LiNbO_3$, generated by excitation of two opposing IDTs acquired at the MEM–LEEM transition, is shown. The SSAW is clearly visible as wavefronts with a periodicity of λ/2 = 4 μm. When only one IDT is excited, a small SSAW component arising from reflections can still be detected [see Fig. 7(*b*)]. The possibility of imaging SSAWs in LEEM opens the path to perform experiments in laboratory setups, as no synchrotron beam is required. As mentioned previously, the positions of nodes and antinodes of a SSAW can be displaced on the sample at will when changing the relative phase of the excitation between the two IDTs. In

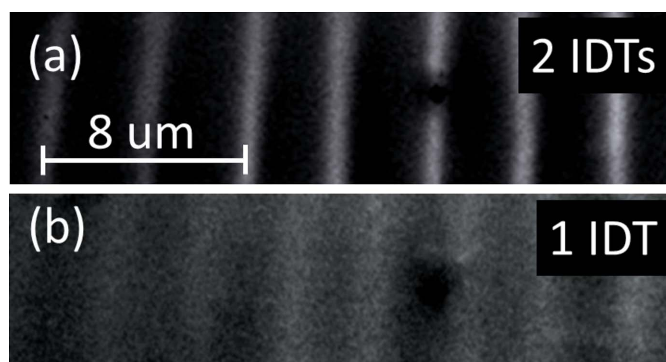

Figure 7
Images of a 500 MHz SAW recorded using the LEEM continuous electron gun, (*a*) upon excitation of both opposing IDTs, generating a strong standing wave as interference pattern, and (*b*) with only one IDT excited, showing a smaller but visible standing wave component.

Video S2 of the supporting information this relative phase is continuously changed, again highlighting the possibility to selectively place a node or antinode in a desired spot on the sample, in order to create a highly local (periodic) excitation.

4. Summary

In conclusion, we describe a stroboscopic method for high-resolution imaging of SAWs in synchrotron-based XPEEM. Through synchronization of the SAWs with the X-ray pulses, time-resolved images with a spatial resolution below 100 nm and temporal smearing below 80 ps can be obtained. The contrast arises from the shift in the low-energy secondary electron spectrum due to the piezoelectric potential of the SAW. The SAW amplitude in the region of interest can thus be quantified by photoelectron spectro-microscopy and translated to strain. General interference of SAWs can be studied and standing and propagating components can be disentangled and quantified by deliberate small detuning of the excitation and the analysis of the produced intensity oscillations. A standing SAW component can also be imaged by LEEM. Our approach is straightforward for frequencies which are multiples of the synchrotron repetition rate (typically 500 MHz), but other frequencies can be used with a suitable timing system (see Appendix *C* for measurements at 125, 250 and 375 MHz). The stroboscopic method can be used to investigate SAWs in detail in very specific configurations, and, thus, allows to fine tune experimental conditions or to help in the design of future SAW devices. It does also provide the grounds to study SAW-excited mechanisms in hetero-structures, triggered by either the SAW-induced strain or the piezoelectric component, in versatile LEEM/PEEM instruments.

APPENDIX *A*
Time/phase resolution of the experimental setup

The phase resolution that can be obtained of the SAWs (in a given point) is limited on the one hand by the spatial resolution in the XPEEM and on the other by the temporal smearing during the averaging of hundreds of millions of partial images. Upper limits for both contributions are determined from the PEEM image shown in Fig. 8(*a*). The lower, solid red line through a 2 μm × 2 μm Ni square represents the region where the lower line scan (profile) in Fig. 8(*b*) (solid red line) is extracted. The spatial resolution under these conditions, as defined by a 15–85% edge jump criterion (shaded grey region) of the Ni square edge, is 100 nm, which would translate into a phase resolution of 4.5° or 25 ps in time for a 500 MHz SAW with $\lambda \simeq 8$ μm if temporal smearing was neglected.

Several factors contribute to the total temporal smearing, such as the X-ray bunch length (20 ps) and dephasing of the X-ray bunches along the orbit (less than 3 ps). However, the main factor is the electronic jitter of the SAW excitation with respect to the master clock which has been measured with an oscilloscope and is approximately 60 ps in the optimum power range (Foerster *et al.*, 2016). Experimentally, an upper limit of the total temporal smearing can be deduced by considering the most detailed feature of the SAW that can be resolved. The electron kinetic energy in Fig. 8(*a*) has been adjusted to reveal a dark line within the bright zone of the SAW between two Ni squares. Such features can be observed within the energy region where the two spectra of Fig. 2(*c*) cross. The upper profile in Fig. 8(*b*) is the line scan taken along the dotted red line in Fig. 8(*a*) through this dark stripe. The grey boxes again graphically represent the resolution; they correspond to 350 nm on the left and 300 nm on the right, respectively. These values translate into a phase (time) resolution of 16° (88 ps)

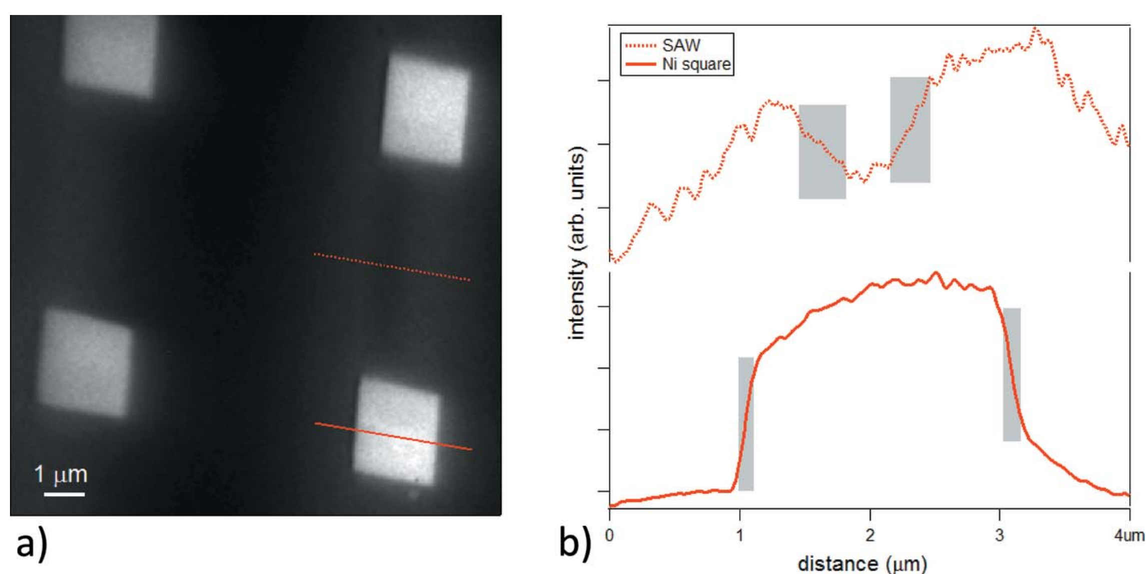

Figure 8
(*a*) XPEEM image used to assess the experimental phase resolution. The dotted and solid lines indicate the regions of the line scans shown in part (*b*). (*b*) Line scans (profiles) demonstrating the spatial resolution (solid line) using the Ni squares as object and determining the time resolution (dotted line) from a feature of the SAW.

on the left and 14° (75 ps) on the right. Note that these values are only an upper limit because the original SAW feature cannot be expected to be infinitively sharp or line-like. A deconvolution with the microscope spatial resolution results in slightly lower values for the temporal smearing alone, *i.e.* 84 ps and 71 ps, respectively, in line with the expectation based on the electronic jitter and the ALBA storage ring filling. Obviously, the values only apply for a spatially small enough zone of interest as the phase in the image is changing with the position along the SAW propagation direction. A measured time resolution clearly below 100 ps constitutes an excellent result in XPEEM.

APPENDIX *B*
Transmission and reflection measurement in IDTs

The reflected signal in opposed IDTs hardly varies with the IDT termination, whether it is terminated by a short circuit, an open circuit or with a standard 50 Ω load (see Fig. 9).

APPENDIX *C*
SAWs at frequencies other than 500 MHz

While the 500 MHz repetition rate of the synchrotron light is the most straightforward choice to investigate SAWs in XPEEM, there are certain applications, for example sample-specific resonances excited by SAWs, where the possibility to access other frequency ranges is desirable. Since the IDTs we use have a fundamental frequency of 125 MHz, in principle, SAWs of most of the multiples of that value can be excited in the samples. In Fig. 10(*b*) we show a PEEM image of a SAW tuned to exactly a quarter of the synchrotron repetition frequency, *i.e.* close to 125 MHz. A clear SAW contrast with 8 µm periodicity is still visible. This may appear surprising at first sight, because the stroboscopic imaging at 500 MHz produces four different images within each SAW period of 8 ns, which are summed (averaged) on the detector. The sum of the SAW surface potential shift of the single images is zero for all points on the sample and, thus, cancel. However, due to the strong nonlinear character of the intensity (electron count rate) versus electron energy [Fig. 2(*c*)], the sum of the intensities still varies with the averaged phase of the SAWs. In general, if I is a nonlinear (strictly speaking non-odd symmetry) function, then $I(a) + I(-a) \neq 2I(0)$ although the amplitudes cancel: $a + (-a) = 0$. Although the wavelength of SAWs at 125 MHz is 32 µm, the periodicity of images in Fig. 10(*b*) is still 8 µm, which reflects the fourfold oversampling of the SAWs by the incoming photon pulses, making it impossible to differentiate phase shifts of 90° of the SAWs at any given moment. In the integer oversampling regime, the

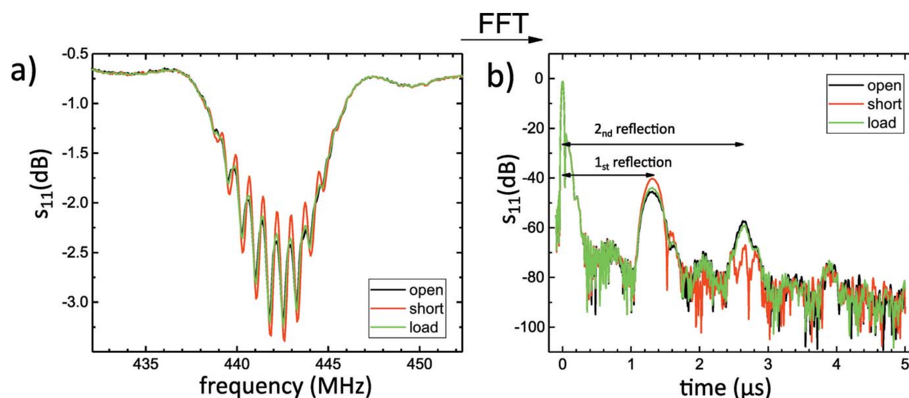

Figure 9
(*a*) Electrical reflection coefficient of an IDT at a resonance frequency of 440 MHz. (*b*) The same signal as in (*a*) in the time space showing the reflected signals that correspond to the initial reflection and first and second reflections in the opposed IDTs. Different terminations of the opposed IDTs are compared: open circuit (black), short circuit (red) and loaded with 50 Ω (green).

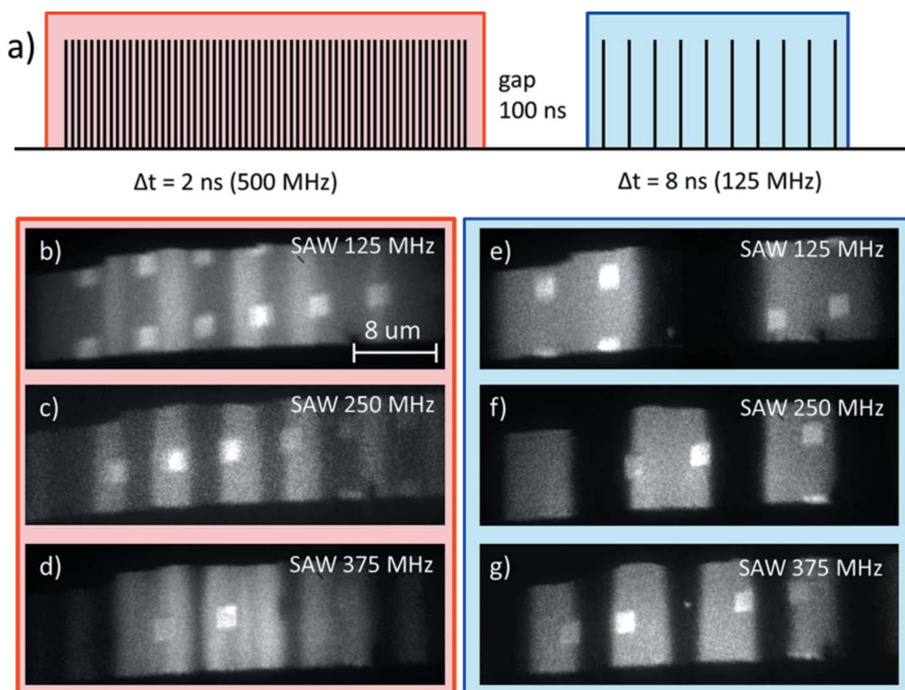

Figure 10
(*a*) Schematic of the hybrid mode filling pattern (intensity versus time) of the synchrotron used to obtain data in this figure. The panels below show XPEEM imaging at lower SAW harmonics of (*b*) 125 MHz, (*c*) 250 MHz and (*d*) 375 MHz imaged in standard multibunch illumination at 500 MHz [red box in (*a*)]. Residual contrast is due to non-linear intensity function of amplitude with the periodicity of 8 µm defined by a stroboscopic imaging rate of 500 MHz. (*e*)–(*g*) Images obtained when using an X-ray illumination rate of 125 MHz [blue box in (*a*)], revealing the SAWs at 32 µm, 16 µm and 12 µm wavelength.

apparent periodicity is rather given by v/f_i = 8 µm, where v is the SAW sound velocity and f_i the imaging frequency, for any SAW frequency. In Figs. 10(*c*) and 10(*d*) we show the corresponding images for SAWs at 250 MHz and 375 MHz. Again some periodic contrast of 8 µm is observed.

Recently, hybrid mode filling patterns have become available at the ALBA synchrotron by single-bunch selective injection (Munoz Horta *et al.*, 2017). A filling pattern containing a part where electron bunches are only in every fourth bucket (125 MHz repetition rate, 8 ns spaced in time) has been made available [Fig. 10(*a*)]. An electron gating device recently installed in the PEEM imaging column, which will be described elsewhere (Aballe *et al.*, 2019), allows selection of either the part with 125 MHz repetition rate or that with 500 MHz repetition rate and switch off the acquisition during the other part. The switching takes place during two 100 ns-long gaps in the filling pattern. Using 125 MHz stroboscopic imaging, the very same SAWs as shown in Figs. 10(*b*)–10(*d*) can be observed in a phase-resolved way as is shown in Figs. 10(*e*)–10(*g*). For the SAW at 125 MHz in panel (*e*) the imaging process is now again fully synchronized like in the case of multibunch illumination with the 500 MHz SAWs discussed so far. In the cases of 250 MHz and 375 MHz excitations, the SAW is undersampled by the X-rays, *i.e.* one partial image is obtained only every second or third SAW cycle, which still provides full phase resolution in the final image.

Acknowledgements

The authors thank Bernat Molas, Abel Fontsere and Oscar Matilla from ALBA electronics for providing the electronic setup, Jordi Prat (ALBA) for assistance in preparing the experiments and Werner Seidel (PDI) for the preparation of IDT structures by lithography. We thank Rafael Cichelero for help in preparing samples at ICMAB.

Funding information

This project was supported by the ALBA in-house research program through projects ALBA-IH2015PEEM and ALBA-IH2017PEEM. The following funding is acknowledged: Ministerio de Economía y Competitividad, Agencia Estatal de Investigación (grant No. RyC-2014-16515 to Ferran Macià; grant No. SEV-2015-0496 to Intitute of Materials Science of Barcelona, ICMAB-CSIC; grant No. MAT2015-69144 to Joan Manel Hernàndez Ferràs, Nahuel Statuto, Ferran Macià; grant No. MAT2015-64110 to Michael Foerster, Lucia Aballe; grant No. MAT2017-85232-R to Blai Casals, Ferran Macià).

References

Aballe, L., Foerster, M., Locatelli, A. *et al.* (2019). In preparation.

Aballe, L., Foerster, M., Pellegrin, E., Nicolas, J. & Ferrer, S. (2015). *J. Synchrotron Rad.* **22**, 745–752.

Auld, B. A. (1973). *Acoustic Fields and Waves in Solids.* New York: Wiley.

Beil, F. W., Wixforth, A., Wegscheider, W., Schuh, D., Bichler, M. & Blick, R. H. (2008). *Phys. Rev. Lett.* **100**, 026801.

Davis, S., Baruth, A. & Adenwalla, S. (2010). *Appl. Phys. Lett.* **97**, 232507.

Foerster, M., Macià, F., Statuto, N., Finizio, S., Hernández-Mínguez, A., Lendínez, S., Santos, P. V., Fontcuberta, J., Hernàndez, J. M., Kläui, M. & Aballe, L. (2017). *Nat. Commun.* **8**, 407.

Foerster, M., Prat, J., Massana, V., Gonzalez, N., Fontsere, A., Molas, B., Matilla, O., Pellegrin, E. & Aballe, L. (2016). *Ultramicroscopy*, **171**, 63–69.

Hernandez, J. M., Santos, P. V., Macià, F., García-Santiago, A. & Tejada, J. (2006). *Appl. Phys. Lett.* **88**, 012503.

Inoue, Y. (2007). *Surf. Sci. Rep.* **62**, 305–336.

Kavalerov, V., Fujii, T. & Inoue, M. (2000). *J. Appl. Phys.* **87**, 907–913.

Kuszewski, P., Camara, I. S., Biarrotte, N., Becerra, L., von Bardeleben, J., Savero Torres, W., Lemaître, A., Gourdon, C., Duquesne, J. Y. & Thevenard, L. (2018). *J. Phys. Condens. Matter*, **30**, 244003.

Lima, M. M. Jr de, Santos, P. V., Kosevich, Yu. A. & Cantarero, A. (2012). *Appl. Phys. Lett.* **100**, 261904.

Mitrelias, T., Kelling, S., Kvon, R. I., Ostanin, V. P. & King, D. A. (1998). *Surf. Sci.* **417**, 97–106.

Molas, B., Aballe, L., Foerster, M., Fontsere Recuenco, A., Matilla, O. & Moldes, J. (2017). *Proceedings of the 16th International Conference on Accelerator and Large Experimental Control Systems (ICALEPCS'17)*, 8–13 October 2017, Barcelona, Spain, pp. 1577–1581. THPHA084.

Munoz Horta, R., Benedetti, G., Lanaia, D., Moldes, J., Perez, F., Pont, M. & Torino, L. (2017). *Proceedings of the 8th International Particle Accelerator Conference (IPAC2017)*, 14–19 May 2017, Copenhagen, Denmark, pp. 2744–2746. WEPAB071.

Rocke, C., Zimmermann, S., Wixforth, A., Kotthaus, J. P., Böhm, G. & Weimann, G. (1997). *Phys. Rev. Lett.* **78**, 4099–4102.

Ruppel, C. C. W. (2017). *IEEE Trans. Ultrason. Ferroelectr. Freq. Control*, **64**, 1390–1400.

Telieps, W. & Bauer, E. (1985). *Ultramicroscopy*, **17**, 57–65.

Thevenard, L., Camara, I. S., Majrab, S., Bernard, M., Rovillain, P., Lemaître, A., Gourdon, C. & Duquesne, J. (2016). *Phys. Rev. B*, **93**, 134430.

Weiler, M., Dreher, L., Heeg, C., Huebl, H., Gross, R., Brandt, M. S. & Goennenwein, S. T. B. (2011). *Phys. Rev. Lett.* **106**, 117601.

Weiler, M., Huebl, H., Goerg, F. S., Czeschka, F. D., Gross, R. & Goennenwein, S. T. B. (2012). *Phys. Rev. Lett.* **108**, 176601.

Wixforth, A. (2003). *Superlattice Microstruct.* **33**, 389–396.